Unsteady Navier-Stokes Simulations of a Rotor Operating in Wake

Zahle, Frederik; Aagaard Madsen, Helge; Sørensen, Niels N.

Published in:
Proceedings

Publication date:
2011

Document Version
Publisher's PDF, also known as Version of record

Unsteady Navier-Stokes Simulations of a Rotor Operating in Wake

Frederik Zahle, Helge Aagard Madsen, Niels N. Sørensen
Wind Energy Division, Risø National Laboratory for Sustainable Energy, DTU, DK-4000 Roskilde, Denmark
frza@risoe.dtu.dk

Abstract

A series of Navier-Stokes simulations have been carried out for the UpWind 5 MW Reference rotor operating in a half-wake situation using the in-house code EllipSys3D. The upstream wake profiles were generated in the aeroelastic code HAWC2's Dynamic Wake Meandering model with a given turbulence intensity (TI) in the free stream. Three TIs were used: 0%, 5% and 10%. The resulting mean wake profiles were subsequently prescribed at the inlet to the CFD simulation in a laminar fashion. An additional case was computed using a more idealised profile consisting of a horizontal step change from 5 m/s to 10 m/s. The half-wake situation caused a large reduction in power production depending on the depth of the upstream velocity deficit. However, the rotor was found to operate at a near constant power coefficient for all four cases compared to the uniform inflow case. In terms of local blade section characteristics it was found that the phase lag was highest moving from the undisturbed inflow into the wake deficit. The extracted induced velocities in the rotor plane showed a strong variation as a function of azimuth. This clearly indicates that in order to handle non-uniform inflows accurately, Blade Element Momentum codes need model induction with an azimuthal dependency.

1 Introduction

Modern wind turbines are frequently placed in clusters, where they for significant periods of time will operate in unsteady inflow conditions caused by wakes from upstream turbines. Together with other flow conditions such as sheared inflow and large scale turbulence the inflow across the rotor swept area is more often than not likely to be non-uniform. On occasions with low ambient turbulence the upstream wake has been observed to be very stable giving rise to high velocity gradients on the wake edge. Figure 1 shows the local flow angle and blade root flap moment measured on an NM80 wind turbine in a situation where it operated in half-wake from a turbine situated 3.1 rotor diameters upstream [5]. The flow angle is seen to vary with up to 12 deg. corresponding to an estimated variation in the axial velocity of 9 m/s.

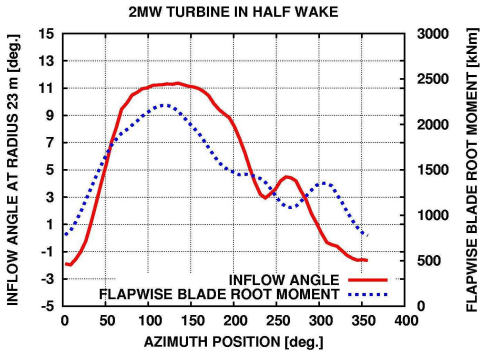

Figure 1: Measured inflow angle and flapwise blade root moment on a 2MW NM80 turbine operating in a half wake situation [5].

In the above experiment and others it has been documented that turbines often operate under conditions with highly non-uniform inflow. The question then arises how well these types of flow situations are modelled in the design codes used by industry. In a BEM context the non-uniform inflow and consequently non-uniform induction have to be handled by an appropriate model. This is by no means trivial, which for the case of inflow shear, has been shown in recent work by Madsen et al. [6] where a number of engineering codes and advanced flow models were compared.

A large body of work exists on wind turbine wakes and turbine wake operation [9, 11, 13, 16]. Common to all these works is that the rotor itself is modelled as either an actuator disc (AD) or using an actuator line (AL) approach, where each blade is represented using body forces. In the AL approach the forces imposed

in the computational domain are generated using a Blade Element model together with appropriate airfoil data. The article by Madsen et al. [6] indicated that also these types of models are associated with some uncertainty due to e.g. the application of tip correction models.

The present work aims to extend the knowledge gathered in Zahle and Sørensen [19] and Madsen et al. [6] where the influence of atmospheric shear was investigated. This work focuses solely on the flow situation where a turbine operates in the half-wake of an upstream turbine. Similarly to the simulations of shear, the non-uniform inflow is prescribed in a steady fashion, i.e. the time varying effects of wake meandering are not included.

Simulations are carried out for one idealised case consisting of a horizontal velocity step from 10 m/s to 5 m/s as well as three half-wake conditions with wake profiles extracted three diameters downstream of a turbine operating in 0%, 5% and 10% turbulence intensity, respectively. A more detailed description of the method is given in Section 3.

The ommision of the meandering process of the upstream wake deficit due to large scale turbulence is a deliberate choice in this work in order to simplify the already very complex flow case. However, it is clear that this simplification renders the results less likely to compare well with actual power outputs of real turbines, since the meandering process has a tendency to smear the steep gradients in the wake deficit. The test cases should make it possible to analyse the possible shortcomings of various properties of BEM codes, in particular their ability to correctly model azimuthally varying induction as well as time delay contributions from the dynamic stall and inflow models.

2 Computational Methods

2.1 Flow solver

All computations in this study were carried out using the flow solver EllipSys3D developed by Michelsen [7, 8] and Sørensen [14]. The EllipSys3D solver is a multiblock finite volume discretization of the incompressible Reynolds-averaged Navier-Stokes (RANS) equations in general curvilinear coordinates. The variables are stored in a collocated grid arrangement, and odd/even pressure decoupling is avoided using the Rhie-Chow interpolation [12]. To solve the coupled momentum and pressure-correction equations the iterative SIMPLE [10] or PISO [2] algorithms are used. For unsteady simulations the solution is advanced in time using a second order iterative time-stepping (or dual time-stepping) method. The convective terms are discretised using the Quadratic Upstream Interpolation for Convective Kinematics Scheme, QUICK [4], and the viscous terms are discretised using the central difference scheme. To accelerate the convergence of the pressure-correction equation a multigrid solution strategy is implemented and the code is fully parallelised using the MPI library. To further accelerate the convergence of the solution, grid and time step sequencing is used. In each level in the grid sequence every second grid point is removed, reducing the number of cells by a factor eight.

2.1.1 The overset grid method

To handle the relative motion between the rotor and the ground the so-called overset grid method is used. In the present implementation by Zahle [18] each group of simply connected blocks is solved using boundary conditions on the overlapping interfaces based on interpolated values of velocity from neighbouring grids using trilinear interpolation. An explicit correction of the conservation error associated with the non-conservative interpolation is implemented, since a divergence free field is required to solve the pressure-correction equation. The correction is placed in internal cells along the overset boundaries and is distributed proportionally to the local mass flux. The solution of the pressure is obtained on the basis of the mass fluxes calculated from the momentum equations.

2.2 Computational Mesh

The 5 MW Reference turbine used in this work has a rotor diameter of 126 m and has a hub height of 90 m. The rotor is modelled without tower, nacelle and spinner and the simulations do not include any elastic deformation of the rotor.

The simulations were all carried out using overset grids. The grid consisted of a total of four overlapping block groups, one body-fitted grid around the rotor and three background grids to resolve the wake and farfield. The surface mesh around each blade of the rotor

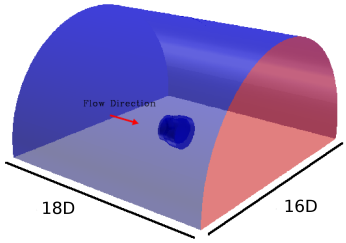

Figure 3: Computational domain around the UpWind 5MW reference turbine.

had 256 cells in the chordwise direction and 128 cells in the spanwise direction and was grown outwards using HypGrid3D [15] to form an O-O topology. The first cell in the boundary layer had a height of 1×10^{-6} m corresponding to a $y+$ of less than 2. This mesh was grown outwards approximately 7 m using 64 cells. This was embedded in a cylindrical mesh with a radius of 78 m and length of 34 m consisting of 96 blocks of 32^3. The third block group covered the wake and had a radius of 88 m and extended 1.25 rotor diameters downstream and contained 80 blocks of 32^3. The outermost blockgroup was semi-cylindrical and extended 8 rotor diameters away from the rotor and consisted of 52 blocks of 32^3. The total grid assembly contained 15×10^6 cells. Figure 2 shows a front- and sideview of the mesh.

In the simulations, the rotor mesh and the innermost cylindrical grid rotated together at the rotational speed of the rotor, with the latter two block groups stationary.

Figure 3 shows the computational domain with overall dimensions. The inflow boundaries are highlighted in blue, while on the bottom ground boundary, a symmetry (slip-wall) boundary condition was applied. A zero-gradient outflow condition was imposed on the downstream boundary shown in red.

2.3 Computational Parameters

All simulations were carried out using the QUICK scheme to discretise the convective terms and the SIMPLE algorithm was used to solve the coupled velocity/pressure equations. In all the simulations the flow was assumed to be fully turbulent using the $k-\omega$ SST model.

At 10 m/s the UpWind rotor has a rotational speed of 1.2 rad/s. However, since the turbine operates in wake, the turbine controller would reduce the rotational speed proportionally to the reduction in power production. Based on HAWC2-aero calculations, the rotational speed was set to 0.92 rad/s, which is the rotational speed used for all flow cases in this paper. Similar to simulations with a sheared inflow, wake-simulations were found to require a significant amount of simulation time to converge towards a periodic solution. To minimise the computational time, grid sequencing and time step sequencing were used by firstly computing the flow on the mesh coarsened by a factor of two in each coordinate direction (grid level 2) with a very coarse time step of 2.2765×10^{-2} with 300 time steps per revolution for 20 revolutions (Gr3). While still on grid level 2, the time step was subsequently refined by a factor of five to 4.553×10^{-3} yielding 1500 time steps per revolution for another 15 revolutions (Gr2). Finally the mesh was refined to the finest grid level (grid level 1) and the time step refined by a factor of two to $\Delta t = 2.2765\times10^{-3}$ (Gr1). Convergence of the solution will be addressed in the Results section.

3 Flow Cases

The wake profiles used in this paper were generated using the recently developed DWM (Dynamic Wake Meandering) model by Madsen et al [6]. The model contains three sub-models: a method to compute the quasi-steady velocity deficit and its development downstream, a model of the downstream wake meandering process, and finally, a model of the added wake turbulence. In the present work the wake profiles were extracted three rotor diameters downstream of a turbine operating in a flow with a given inflow turbulence and no mean wind shear. The extracted velocity profiles were subsequently time-averaged, since they were applied as a stationary profile to the CFD simulations.

Three wake flow cases were chosen with 0%, 5% and 10% turbulence intensity. Although the 0% scenario is unlikely to occur very often, virtually laminar flow conditions do occur at night time under highly stratified flow conditions which will be associated with a strong atmospheric shear. In the present flow cases, however, shear has been omitted. The wake in all three cases were horizontally offset 60 m from the rotor center. An additional more idealised case was setup since it quickly became evident that the azimuthally varying load patterns using actual wake shapes were very

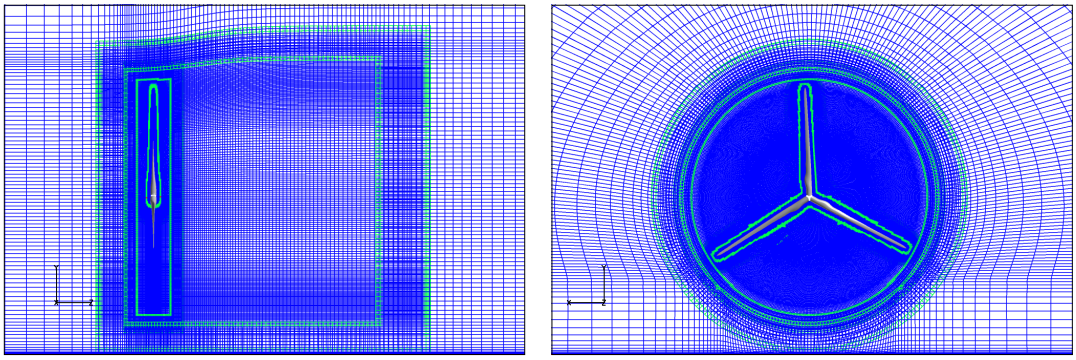

Figure 2: Sideview and frontview of the mesh around the UpWind 5MW reference turbine generated with a hub height of 90 m.

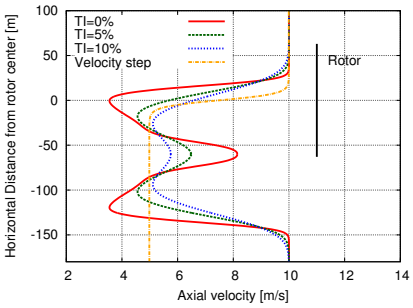

Figure 4: Wake profiles used as inflow for the simulations.

complex. This case consisted of a horizontal velocity step from 5 m/s to 10 m/s with the transition between the two velocity levels roughly corresponding to the 0% TI case. The velocity profile was defined by the following function:

$$w(x) = .75 - .25\left(-\tanh(\frac{x \cdot 8.78044}{63.0})\right) \quad (1)$$

Figure 4 shows the four velocity profiles applied at the inlet. Note that the first three cases are applied as a rotationally symmetric profile, whereas the velocity step is constant in the vertical direction. Figure 5 shows the inflow profiles in a contour plot with the rotor drawn in for reference.

4 Basic Definitions

The following sections present all results in terms of sectional normal and tangential forces, as well as mechanical power production and thrust. The normal and tangential forces are defined relative to the rotor plane; that is normal to and tangential to the rotor plane and is composed of both pressure and skin friction components. Likewise the integrated thrust and torque of the rotor also comprise both skin friction and pressure contributions. Results are presented in a polar grid, where the azimuth angle is defined as zero when the blade is pointing vertically upwards, and positive in a clockwise rotation.

The power available in the wind is $P_{avail} = \frac{1}{2}\rho w^3 A_{swept}$, where w is the axial flow velocity and A_{swept} is the rotor swept area. When dealing with non-uniform inflows it is not meaningful to define the power coefficient relative to some reference velocity defined at e.g. hub height, since this rarely reflects the actual energy content in the flow. Rather, the power coefficient should be defined relative to the actual energy content over the rotor swept area. The mechanical power coefficient, C_P is thus defined as:

$$C_P = \frac{P_{mech}}{\frac{1}{2}\rho \int_0^R \int_0^{2\pi} w(r,\phi)^3 dr d\phi} \quad (2)$$

where r is the radius and ϕ is the azimuthal angle. Likewise, we define the thrust coefficient as:

$$C_T = \frac{T}{\frac{1}{2}\rho \int_0^R \int_0^{2\pi} w(r,\theta)^2 dr d\phi} \quad (3)$$

where T is the rotor thrust.

The local power coefficient is defined as follows:

$$C_{P-local} = \frac{\Delta P}{\frac{1}{2}\rho w(r,\theta)^3 \Delta A} = \frac{F_t \omega \cdot nb}{\rho \pi w(r,\theta)^3} \quad (4)$$

where F_t is the local blade force per meter tangential to the rotor plane, ω is the rotational speed, and nb is the number of blades. This definition assumes that the local force is constant along an annular element, which for a non-uniformly loaded disc it clearly is not. As such it is not comparable to the global power coefficient defined in 2 for non-uniformly

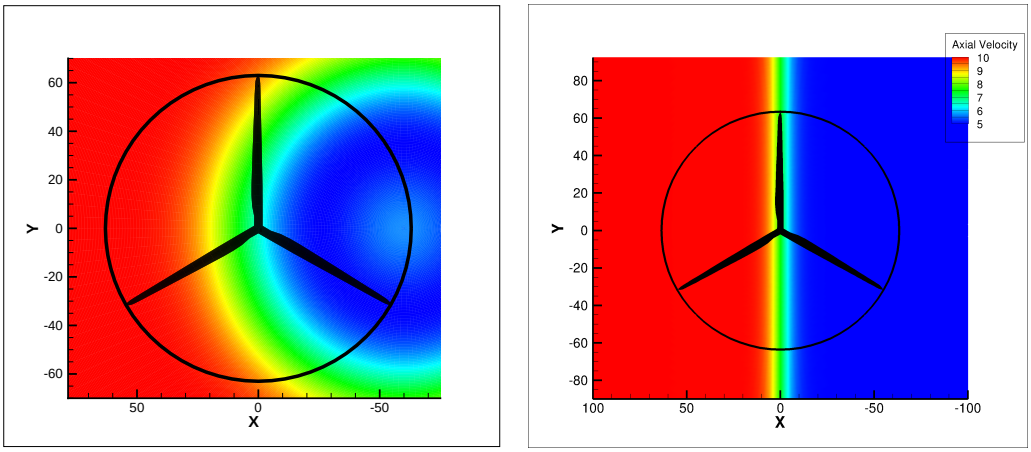

Figure 5: Contour plot of the inflow profiles for the 10% TI case (left) and the velocity step case (right).

Grid	Torque (kNm)	Thrust (kN)
Gr3	2079.95 (5.8%)	353.23 (2.1%)
Gr2	2032.72 (3.4%)	344.95 (0.3%)
Gr1	1966.78 (-)	346.07 (-)

Table 1: Integral forces for the velocity step case at each of the three grid/time step levels.

loaded rotors, however, it provides insight into the local power extraction across the rotor disc.

The local thrust coefficient is similarly defined as:

$$C_{T-local} = \frac{F_n \Delta r}{\frac{1}{2}\rho w(r,\theta)^2 2\pi r \Delta r} = \frac{F_n}{\rho w(r,\theta)^2 \pi r} \quad (5)$$

where F_n is the local blade force per meter normal to the rotor plane, Δr is the width of the annular element.

5 Results

5.1 Convergence Study

Figure 6 shows a typical time history of the torque for a wake-flow case, here showing the ten revolutions at the finest grid level and time step (Gr1). Table 1 shows the rotor thrust and power production for the velocity step case for each level of the time step and grid level refinement, Gr3, Gr2, and Gr1. As is evident the integrated forces are predicted quite accurately even at the coarsest time step level on grid level 2, resolved by only 300 timesteps.

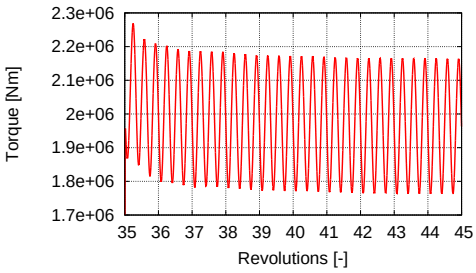

Figure 6: Time history of the torque at the finest grid level and time step.

5.2 Case Comparison

Figure 7 shows the blade root flapwise and edgewise moments over one revolution, comparing the four test cases. Comparing the flapwise and edgewise moments it is evident that the edgewise moment is significantly more reduced then the flapwise moment when the blade is submerged in the wake from the upstream turbine. The velocity step and the 0% TI cases are clearly the most severe cases of the four, since the gradients in the inflow correspond to an inflow with zero turbulence. In the velocity step case we can observe an overshoot of the flapwise moment as the blade passes through 0 deg. azimuth and 180 deg. azimuth, which is not evident in the tangential force. In the 0%, 5% and 10% TI cases we see a progressive increase in the smearing of the effect of the local speedup in the center of the upstream wake, as well as a reduction in the force gradients coming in and out of the shear.

Turning to the integral loads averaged over one revolution, the reader is reminded of the

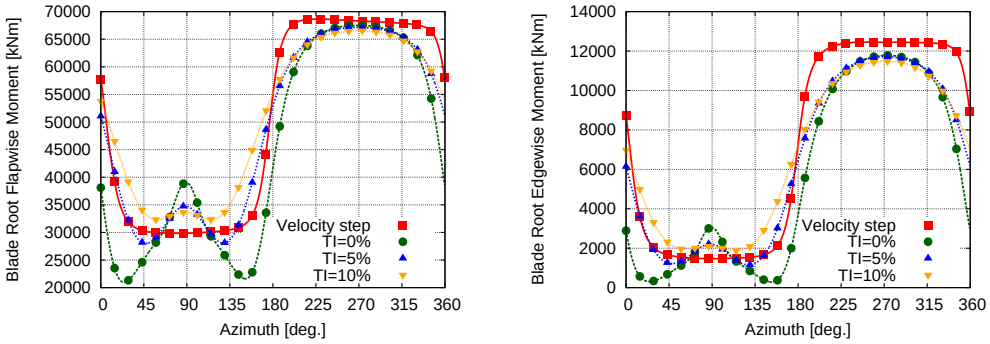

Figure 7: Blade root flapwise and edgewise moments for the four cases over one revolution.

definition of the power and thrust coefficients in Equations 2 and 3, which will be used in the following analysis. Table 2 shows the rotor thrust and mechanical power, with corresponding coefficients of C_T and C_P.

The reduction in power production and thrust is largely identical for the velocity step and the 10% TI cases, which is seen to decrease further with decreasing turbulence intensity. It is, however, interesting to see that besides small decreases for the 0% TI case the power coefficient is slightly increased in the half-wake cases compared to the uniform inflow case. In the Discussion we will look further into the local power extraction across the rotor disc.

Figure 8 shows the normal and tangential force distributions along the blade as a polar plot showing the azimuthal variation of the forces over a full revolution for all four cases. Figure 9 shows the force for four specific azimuthal positions, 0 deg, 90 deg, 180 deg. and 270 deg.

The first test case that is discussed is the idealised case consisting of a horizontal velocity step from 5 m/s to 10 m/s. As opposed to the actual wake cases the inflow velocity is constant in the vertical direction, with the consequence that a blade experiences the velocity change simultaneously along the entire span at 0 deg. and 180 deg. azimuth. For both the normal and tangential forces there is a difference between the load at the 0 deg. and 180 deg. positions, most pronounced in the tangential force. This difference, however, is associated with fairly small phase lag, which due to the large gradient in the force results in a large difference. From Figure 7 the phase lag was found to be 4.3 deg at the 0 deg. blade position. At the 180 deg. position the lag was found to be only 0.5 deg.

The most severe of the flow cases was the case with the zero turbulence profile. As is evident from Figure 4 the velocity in the profile is reduced approximately 64% in the deepest part of the deficit. As shown in Figures 8 and 9 the depth of the deficit results in the blade barely producing any power as it passes through the deficit. In fact, a visualisation of the flow revealed that the velocity is negative in the wake, causing tip vortices from the previous blades to interact with the blade in the 0 deg. to 180 deg. azimuth range. The high degree of complexity of the flow makes it unsuitable to compare against BEM codes, since these codes cannot model such high thrust coefficients. As opposed to the idealised case, the normal and tangential forces are higher at the 180 deg. azimuth position compared to 0 deg. position, which is unexpected, since a pure dynamic stall effect would give rise to a phase lag.

Turning to the cases with 5% and 10% turbulence intensity, we see that the blade forces are now significantly more smeared as a result of the lower gradients in the upstream wake profiles. The apparent phase lead on the outer sections of the blade in the normal and tangential forces is also seen in these two cases. Additionally, we see that the outermost blade sections appear to contribute with negative torque in the 180 deg. azimuth region.

5.3 Extraction of Induced Velocities

The induced velocities in the rotor plane are relevant particularly in a BEM context, since the induced velocities determine the local angle of attack that in turn is used to look up local aerofoil forces on the blade section. In a CFD simulation the induced velocities can be extracted using the so-called *reduced ax-*

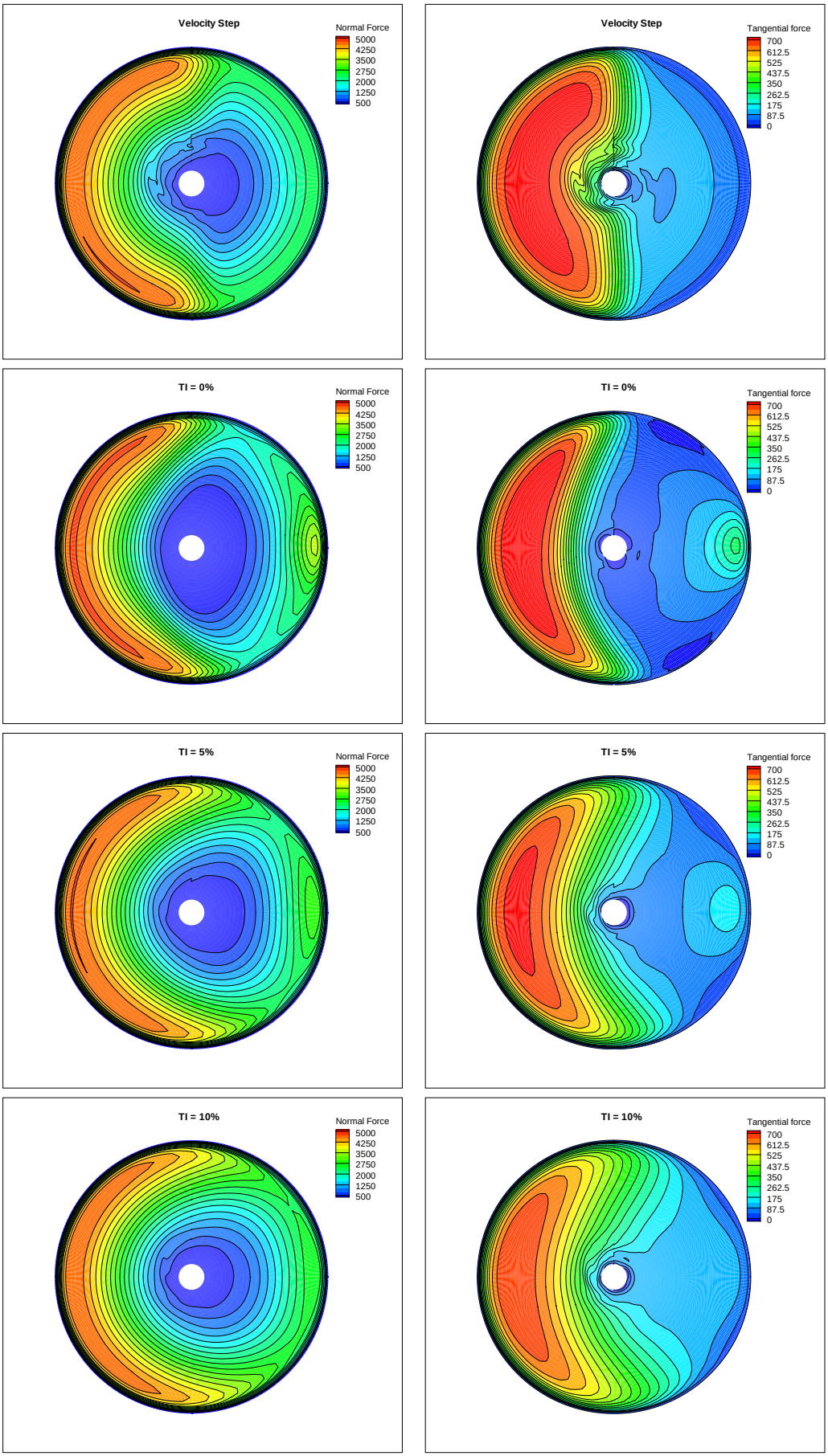

Figure 8: Blade force normal and tangential to the rotor plane for the four half-wake cases shown as a polar contour plot over a complete revolution.

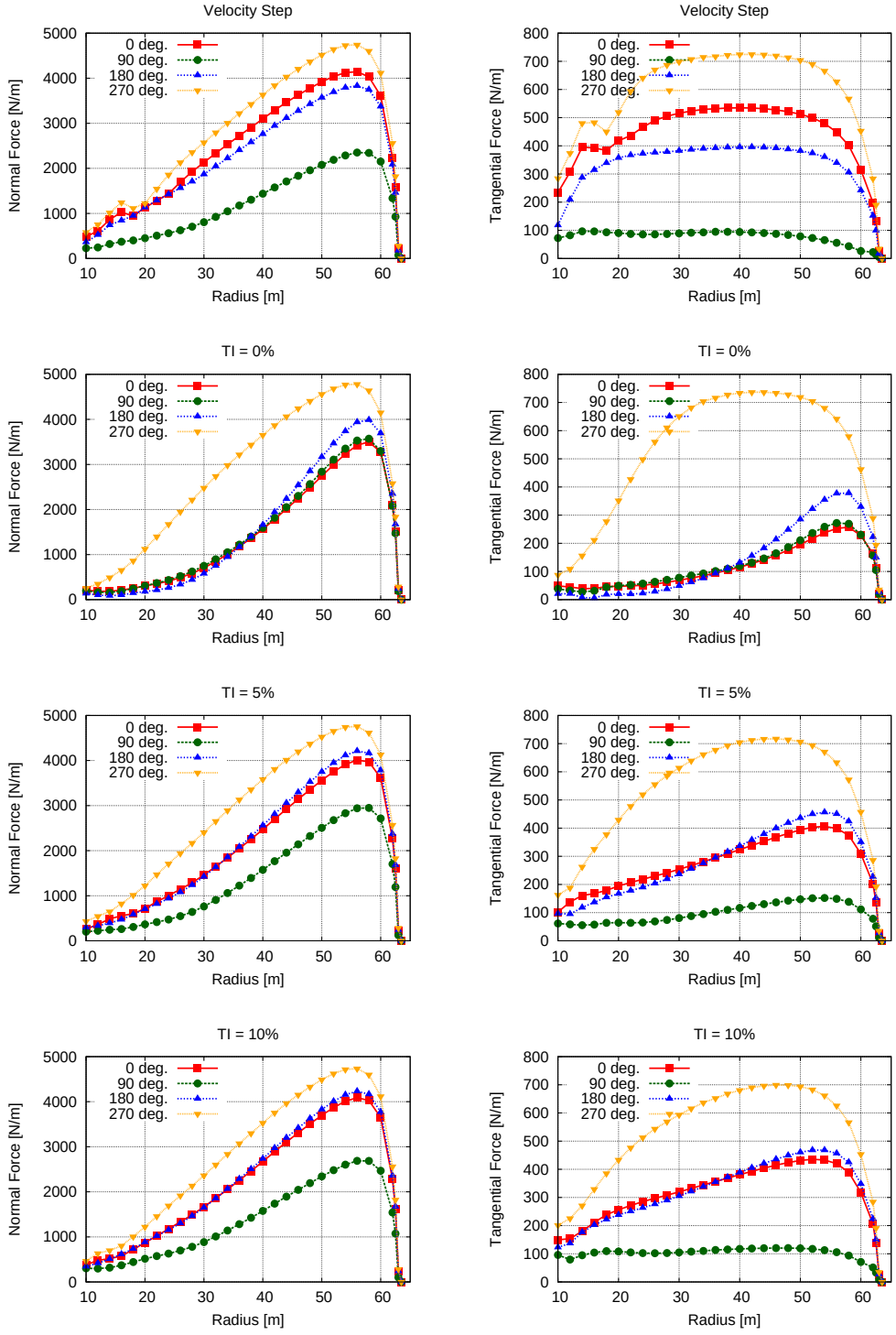

Figure 9: Blade force normal to the rotor plane for the four half-wake cases for four azimuthal angles.

Cases	Power (kW)	C_P	Thrust (kN)	C_T
Uniform (0.92)	3329	0.436	479.7	0.628
Step	1810 (-45.6%)	0.440 (0.92%)	349.9 (-27.1%)	0.738 (17.5%)
TI=0%	1494 (-55.1%)	0.429 (-1.6%)	295.8 (-38.3%)	0.732 (16.6%)
TI=5%	1711 (-48.6%)	0.444 (1.8%)	330.4 (-31.1%)	0.731 (16.4%)
TI=10%	1809 (-45.7%)	0.450 (3.2%)	346.0 (-27.9%)	0.733 (16.7%)

Table 2: Power and thrust of the turbine for the four half-wake cases compared to uniform inflow.

ial velocity method outlined by Johansen and Sørensen [3], which was originally proposed by Hansen et al. [1]. For non-uniform inflow instead of using the azimuthally averaged velocity along an annular element the time averaged velocities in discrete points in a fixed reference frame have to be used.

In this work we only present the extracted induced velocities for the idealised case with the velocity step from 5 m/s to 10 m/s. The induced velocities are extracted at four azimuthal positions: 0 deg., 90 deg., 180 deg., and 270 deg.. Figure 10 shows the induced axial, tangential and radial velocities along the blade span.

5.4 Flowfield

Figure 11 shows a contour plot of the axial velocity in a horizontal plane for the 0% TI case that shows the upstream wake profile and the interaction with the rotor. The wake expands considerably more on the side of the upstream wake than on the undisturbed side, with the result that the wake destabilizes further downstream as a result of the high thrust coefficient.

Figures 12 and 13 show the flowfield for the 0% and 10% TI cases, which clearly illustrate the skewing of the tip vortices due to the non-uniform flowfield. In the 0% case, the depth of the deficit causes the blade to interact with the tip vortices from the previous blades due to the negative velocity in the wake, whereas the skewing is less severe for the 10% case.

Finally, we turn to the downstream development of the wake. Figure 14 shows the axial velocity in the wake at four downstream planes: one, two, three and four rotor diameters (D) downstream. Due to the rotation of the wake the non-uniform wake deficit is swirled in a counter-clockwise motion causing low velocity flow from the right side of the wake to mix with the higher velocity fluid from the left side. The wake is seen to destabilize approximately one and a half diameters downstream resulting in further mixing of the two wakes.

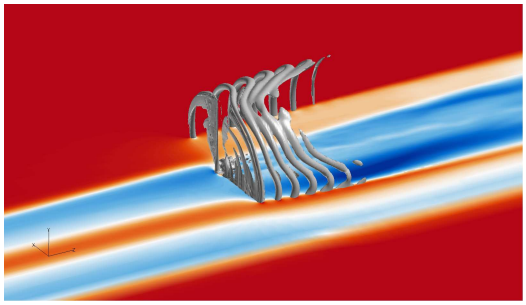

Figure 12: Contour plot of the axial velocity in a horizontal plane through the rotor center and iso-surface of vorticity magnitude for the 0% turbulence intensity case.

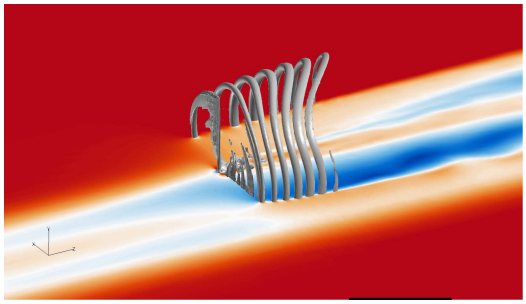

Figure 13: Contour plot of the axial velocity in a horizontal plane through the rotor center and iso-surface of vorticity magnitude for the 10% turbulence intensity case.

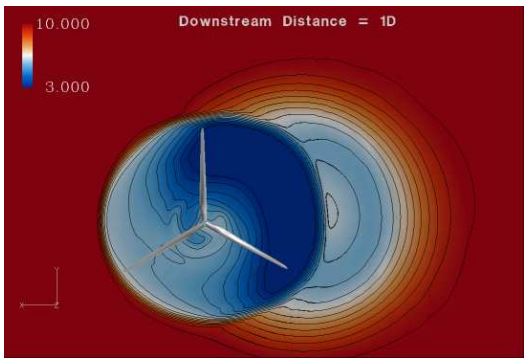

Figure 14: Axial velocity one, two, three and four diameters downstream of the rotor for the 10% TI case (Click on image to animate).

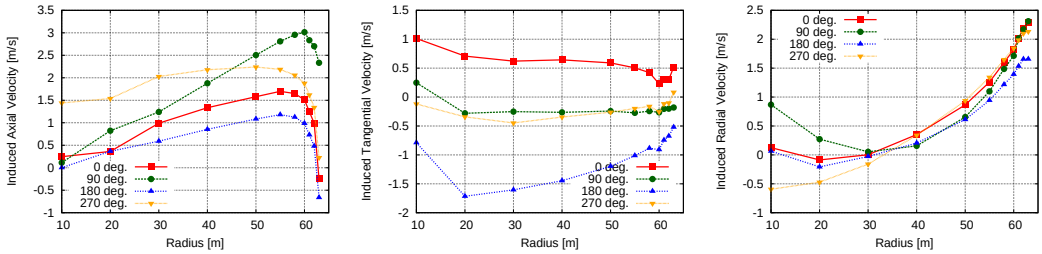

Figure 10: Axial induced velocity as function radius at four azimuthal positions for the rotor operating in strong shear at 8 m/s.

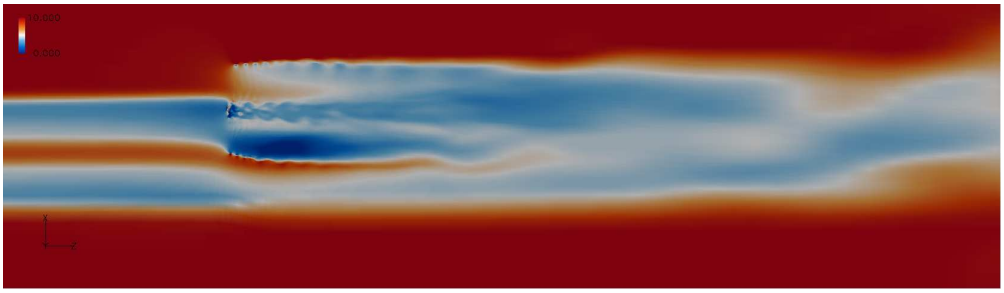

Figure 11: Contour plot of the axial velocity in a horizontal plane though the rotor center for the 0% turbulence intensity case also showing an iso-surface of vorticity magnitude.

6 Discussion

This work is a continuation of the work presented in Zahle and Sørensen [19], where the effect of strong atmospheric shear was investigated for the same rotor used in this paper. In the paper it was shown that the induction varied significantly across the rotor disc indicating that azimuthally varying induction should be implemented in BEM codes when run with non-uniform inflow.

In the present simulations the induced velocities were extracted for the idealised velocity step case. Figure 10 shows the three components of the induced velocity along the blade at four azimuthal positions. As expected, the induced axial velocity differs significantly between the 90 deg. and 270 deg. positions with a very high induced velocity in the region where the rotor operates in wake. The induced radial velocities indicate that a redistribution of the upstream velocity field takes place with high velocity fluid being pushed from the undisturbed high velocity part of the inflow towards the low velocity part of the inflow. This phenomenon was also observed for the rotor operating in shear and was also identified by Troldborg et al. [17] in their actuator disc simulations. The redistribution is seen in the tangential induced velocities with a large negative velocity at 0 deg. azimuth and oppositely a positive induced tangential velocity at 180 deg. azimuth.

The apparent redistribution of the inflow is also visible in the distribution of the local power and thrust coefficients as shown in Figure 15. As is evident, the rotor operates at a fairly constant $C_{P-local}$ in both the low and high velocity regions. At the interface between the the two regions, however, $C_{P-local}$ reaches values above one, which is hypothesized to be caused by the aforementioned velocity redistribution. The locally higher axially induced flow combined with a change in the tangentially induced velocity gives rise to a local increase in angle of attack. The increase is larger at the top since the induced tangential velocity contributes to an increase in angle of attack at the top, whereas it has the opposite effect at the bottom. The same trend is seen for the local thrust coefficient which is also shown in 15 (right). This local increase in $C_{P-local}$ could be related to the increases in C_P shown in Table 2. It is also seen that the rotor operates at a significantly higher $C_{T-local}$ when in wake from the upstream turbine.

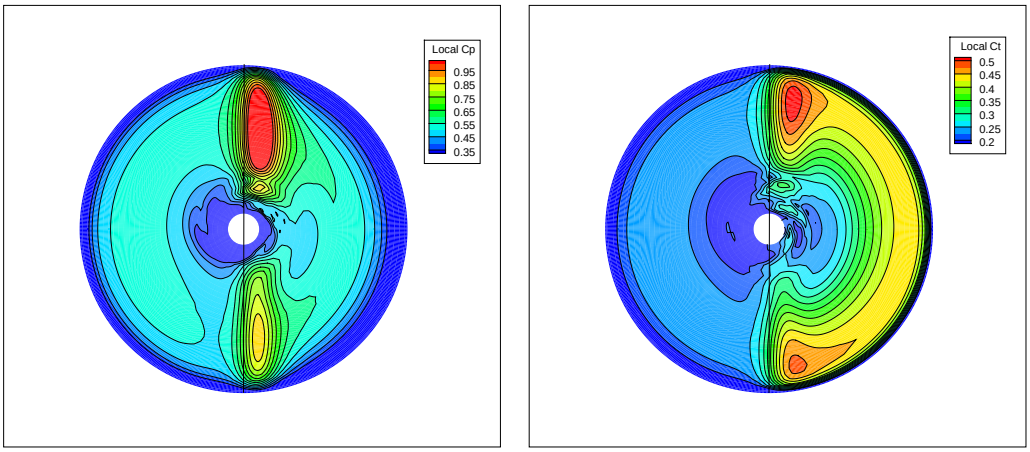

Figure 15: Contour plot of the local power and thrust coefficients over one revolution for the velocity step case.

7 Conclusions

A series of simulations of a fully resolved rotor operating in a half-wake situation have been carried out investigating the effect of different upstream wakes on the loads on a turbine. It was found that increased turbulence intensity in the upstream wake profile gave rise to higher power production as was expected. The power coefficient was found to increase slightly for three of the four wake cases compared to the uniform inflow computation. The thrust coefficients increased for all four cases, but were constant for the different wake profiles.

Induced velocities were extracted for the velocity step case, which showed a significant variation in induction across the rotor. The induced velocities also revealed a large cross-flow component from the high velocity region to the low velocity region. This cross flow component was hypothesized to be related to the increases in C_P, also supported by plots identifying locally very high values of $C_{P-local}$.

The complexity of the half-wake situation was illustrated with various snapshots of the flowfield showing for the 0% TI case interaction of the blades with the tip vortices from the previous blades. The combined wakes destabilised from about 1D-2D downstream of the rotor due to the assymmetry and high expansion of the rotor wake.

Acknowledgements

The majority of the work presented in the this paper has been carried out within work package 2 of the UpWind project, funded by the European Commission. The work was also partly funded by the Danish Council for Strategic Research (DSF) under contract 2104-09-0026, Center for Computational Wind Turbine Aerodynamics and Atmospheric Turbulence. Computations were made possible by the use of the PC-cluster Thyra provided by DCSC and the Risø-DTU ceontral computing facility.

References

[1] M. O. Hansen, N. N. Sørensen, J. N. Sørensen, and J. A. Michelsen. Extraction of lift, drag and angle of attack from computed 3-D viscous flow around a rotating blade. In *Proceedings of European Wind Energy Conference*, page 499–501, Dublin, 1997.

[2] R. I. Issa. Solution of the implicitly discretised fluid flow equations by operator-splitting. *journal of Computational Physics*, 62:40–65, 1985.

[3] J. Johansen and N. N. Sørensen. Aerofoil characteristics from 3D CFD rotor computations. *Wind Energy*, 7(4):283–294, 2004. doi: $10.1002/\mathrm{we}.127$.

[4] B. Leonard. A stable and accurate convective modelling procedure based on quadratic upsteam interpolation. *Computer Methods in Applied Mechanics and Engineering*, 19:59–98, 1979.

[5] H. A. Madsen. Influence of wind shear on rotor aerodynamics, power and loads.

inC. Bak: Research in Aeroelasticity EFP-2006. Technical Report Risø-R-1611(EN), RisøNational Laboratory for Sustainable Energy DTU, Roskilde, July 2007.

[6] H. A. Madsen, G. C. Larsen, T. J. Larsen, N. Troldborg, and R. Mikkelsen. Calibration and validation of the dynamic wake meandering model for implementation in an aeroelastic code. *Journal of Solar Energy Engineering*, 132(4):041014, 2010. doi: $10.1115/1.4002555$.

[7] J. A. Michelsen. Basis3D—a platform for development of multiblock PDE solvers. Technical Report AFM 92-05, Technical University of Denmark, 1992.

[8] J. A. Michelsen. Block structured multigrid solution of 2D and 3D elliptic PDEs. Technical Report AFM 94-06, Technical University of Denmark, 1994.

[9] R. Mikkelsen. *Actuator Disc Methods Applied to Wind Turbines*. Mek-fm-phd 2003-02, Technical University of Denmark, 2003.

[10] S. V. Patankar and D. B. Spalding. A calculation procedure for heat, mass and momentum transfer in three-dimensional parabolic flows. *International Journal of Heat and Mass Transfer*, 15:1787–1806, 1972.

[11] P.-E. Réthoré. *Wind Turbine Wake in Atmospheric Turbulence*. PhD thesis, Aalborg University, 2009.

[12] C. M. Rhie and W. L. Chow. Numerical study of the turbulent flow past an aerofoil with trailing edge separation. *AIAA journal*, 21:1525–1532, 1983.

[13] J. N. Sørensen and W. Z. Shen. Numerical modelling of wind turbine wakes. *Journal of Fluids Engineering*, 124:393–399, 2002.

[14] N. N. Sørensen. General purpose flow solver applied to flow over hills. Technical Report Risø-R-827(EN), Risoe National Laboratory, 1995.

[15] N. N. Sørensen. HypGrid2D—a 2-D mesh generator. Technical report, Risø-R-1035(EN), Risoe National Laboratory, 1998.

[16] N. Troldborg. *Actuator Line Modeling of Wind Turbine Wakes*. PhD thesis, Technical University of Denmark, 2008.

[17] N. Troldborg, M. Gaunaa, and R. Mikkelsen. Actuator Disc Simulations of Influence of Wind Shear on Power Production of Wind Turbines. In *The Science of Making Torque from Wind*, 2010.

[18] F. Zahle. *Wind Turbine Aerodynamics Using an Incompressible Overset Grid Method*. PhD thesis, Imperial College, London, 2006.

[19] F. Zahle and N. N. Sørensen. UpWind: Navier-Stokes Rotor Flow Simulations with Ground Proximity and Shear. In *The Science of Making Torque from Wind*, Heraklion, Greece, 2010.